JOURNAL OF SPACECRAFT AND ROCKETS
Vol. 46, No. 4, July–August 2009

Autonomous Midcourse Navigation for Lunar Return

Renato Zanetti*
Charles Stark Draper Laboratory, Inc., Houston, Texas 77058

DOI: 10.2514/1.41769

Autonomous navigation systems provide the vehicle with estimates of its states without ground support. This work develops an autonomous navigation architecture for lunar transfer using optical sensors and celestial navigation. Measurement and error models are developed for two classes of celestial measurements, the elevation of known stars from the Earth's or moon's limb, and the apparent radius of the Earth or moon. Monte Carlo methods are used to support the development of measurement error models. The proposed architecture is tested with linear covariance techniques; navigation errors and trajectory dispersions are obtained to confirm the feasibility of the approach. The navigation system is required to provide 0.5 deg flight-path angle accuracy at entry interface for mission safety. The simulation results show that the proposed autonomous navigation system meets the reentry safety requirement.

Nomenclature

b, $\mathbf{b}$	=	bias states
c	=	speed of light
$\mathbf{e}$	=	estimation error
$\mathbf{F}$	=	Jacobian of state dynamics
$\mathbf{f}$	=	state dynamics
$\mathbf{H}$	=	measurement mapping matrix
$\mathbf{i}$	=	unit vector
$\mathbf{L}$	=	noise shaping matrix
$\mathbf{N}$	=	rotational maneuver's noise covariance
$\mathbf{P}$	=	estimation error covariance
$\bar{\mathbf{P}}$	=	environment dispersion covariance
$\hat{\mathbf{P}}$	=	navigation dispersion covariance
$\mathbf{Q}$	=	process noise spectral density
$\mathbf{Q}$	=	spectral density of $\boldsymbol{\nu} - \boldsymbol{\upsilon}$
$\mathbf{Q}$	=	spectral density of $\boldsymbol{\upsilon}$
$\mathbf{R}$	=	measurement error covariance
R_P	=	radius of planet
$\mathbf{r}$	=	vehicle's position vector
$\mathbf{T}$	=	rotation matrix
t	=	time
$\mathbf{v}$	=	vehicle's velocity vector
$\mathbf{x}$	=	true state
$\bar{\mathbf{x}}$	=	nominal state
$\hat{\mathbf{x}}$	=	estimated state
Γ	=	Jacobian of the flight-path angle
γ	=	flight-path angle
$\boldsymbol{\gamma}_m$	=	maneuver misalignment error state
$\delta\mathbf{x}$	=	environment dispersion
$\delta\hat{\mathbf{x}}$	=	navigation dispersion
ϵ	=	star-elevation angle
$\boldsymbol{\zeta}$	=	rotational maneuver's noise
η, $\boldsymbol{\eta}$	=	measurement noise
$\boldsymbol{\theta}$	=	rotation vector parameterization of the inertial to vehicle body rotation
$\boldsymbol{\nu}$	=	process noise
Π	=	augmented dispersions covariance matrix
ρ	=	apparent angular radius
σ	=	standard deviation
$\boldsymbol{\sigma}_m$	=	maneuvers scale factor error state
$\boldsymbol{\upsilon}$	=	difference between nominal and estimated dynamics
φ	=	angle of the planet's arc inside the field of view
Ψ	=	event trigger constraint
Ψ_x	=	Jacobian of event trigger constraint

Subscripts

e	=	event
h	=	horizon
m	=	translational maneuver
p	=	planet
r	=	rotational maneuver
s	=	star
se	=	star elevation
ss	=	substellar
st	=	star tracker
v	=	vehicle

Functions

$[\cdot\times]$	=	function returning the cross product skew symmetric matrix
unit$(\cdot)$	=	function returning the normalized vector

I. Introduction

VEHICLES navigating to or from the moon usually rely on ground tracking and ground updates to perform the insertion and correction maneuvers. A natural advancement in technology is autonomy. The Orion vehicle, for example, is required to autonomously return to Earth if communication with the ground is lost. When ground tracking estimates are unavailable to the onboard targeting algorithm an alternative navigation strategy is needed. Optical navigation is an attractive source of information for this emergency scenario. This study focuses on navigating in cislunar space, when terrain measurements are unavailable. From images of Earth, moon, and stars two types of measurements can be generated: the elevation of a star from the planet's limb and the angular radius of the planet.

Recent studies focus on the lunar orbit determination problem [1,2]. Tuckness and Young consider autonomous navigation for lunar transfers [3]. Their analysis focuses on azimuth and elevation measurements of the Earth, moon, and sun. Two star-elevation measurements relative to the planet's limb provide similar information as azimuth and elevation measurements of the planet's centroid from the sensor's boresight. However, star-elevation measurements are the preferred approach for two reasons. First, multiple stars can be processed simultaneously, and the redundant information effectively filters out some noise. Second, the method used here does not depend on the attitude of the spacecraft, or on the misalignments of the

Presented as Paper 6758 at the AIAA/AAS Astrodynamics Specialists Conference, Honolulu, HI, 18–21 August 2008; received 7 November 2008; revision received 13 March 2009; accepted for publication 17 April 2009.

*Senior Member of the Technical Staff, GN&C Manned Space Systems, 17629 El Camino Real Suite 470; rzanetti@draper.com. Member AIAA.

sensors, reducing the possible error sources. In this work, a coupled analysis of navigation errors and trajectory dispersions is performed. The performance of the navigation system is evaluated with mission success criteria.

This investigation specifically addresses the transfer from the moon to the Earth. In an emergency situation, during a loss of communication scenario, the primary objective is the safety of the crew. This subsequently translates into a flight-path angle requirement at entry interface (EI) for a direct entry. A direct entry, as opposed to a skip entry, reduces the risk of the capsule bouncing back into space, and allows for a greater margin on the flight-path angle at EI.

The accuracy of the flight-path angle at EI is driven by several factors including the navigation, targeting, and burn execution errors at the time of the last midcourse maneuver, and unaccounted trajectory perturbations between the last midcourse maneuver and EI. Apollo missions tolerated a maximum flight-path angle error at EI of ± 1 deg, with half of this error allocated to navigation. The same criteria is employed in this study. Specifically, a 0.5 deg 3σ flight-path angle error mapped at EI is required at the time the last midcourse correction is targeted.

The primary objective of this investigation is to model the sensors and analyze the navigation system to ensure that it meets the required safety performance. To that end, mathematical models are developed for the optical measurements. In addition, a strategy for using these measurements is devised. Lastly, the feasibility and performance of the resulting optical navigation system are analyzed.

II. Linear Covariance Analysis

This investigation is performed using linear covariance (LinCov) analysis techniques [4,5]. The state vector is composed of

$$\mathbf{x} = \{\mathbf{r}^T \ \mathbf{v}^T \ \boldsymbol{\theta}^T \ \mathbf{b}_m^T \ \boldsymbol{\sigma}_m^T \ \boldsymbol{\gamma}_m^T \ \mathbf{b}_r^T \ b_{\text{st}} \ b_{\text{ss,earth}} \ b_{\text{ss,moon}} \ b_{h,\text{earth}} \ b_{h,\text{moon}}\}^T \tag{1}$$

The nominal trajectory is obtained by integrating the nominal dynamics model with an Encke–Nystrom method [6]. Neither the rotation vector $\boldsymbol{\theta}$ nor its uncertainty are integrated in this analysis. The nominal attitude is known at any time and it does not need to be calculated. The attitude estimation error covariance is constant and is driven by the star tracker accuracy. The attitude navigation dispersion covariance is constant and is given by the attitude control deadband. The attitude environment dispersion covariance is constant and obtained from the preceding two quantities assumed uncorrelated. Before the star elevation is determined, the vehicle slews in preparation for measurement acquisition. This attitude maneuver is performed by the onboard thrusters and is assumed to be instantaneous. Because of thruster misalignment, this maneuver adds uncertainty to the translational states. After the batch of measurements is available the vehicle returns to its nominal attitude. In linear covariance analysis, the difference between the true state and the nominal state is defined as the environment dispersion

$$\delta\mathbf{x} \triangleq \mathbf{x} - \bar{\mathbf{x}} \tag{2}$$

The difference between the estimated state and the nominal state is defined as the navigation dispersion

$$\delta\hat{\mathbf{x}} \triangleq \hat{\mathbf{x}} - \bar{\mathbf{x}} \tag{3}$$

Finally, the difference between the true state and the estimated state, is defined as the estimation error, sometimes referred to as the onboard error

$$\mathbf{e} \triangleq \mathbf{x} - \hat{\mathbf{x}} \tag{4}$$

Following the standard Kalman filter assumptions, the difference between the nominal and estimate models is represented with zero-mean white noise. The estimated state evolves as

$$\dot{\hat{\mathbf{x}}} = \mathbf{f}(\hat{\mathbf{x}}) \tag{5}$$

where $\mathbf{f}$ is a nonlinear function representing the system dynamics as modeled by the filter. The evolution of the nominal state is modeled as

$$\dot{\bar{\mathbf{x}}} = \bar{\mathbf{f}}(\bar{\mathbf{x}}) = \mathbf{f}(\bar{\mathbf{x}}) + \boldsymbol{\upsilon} \tag{6}$$

where $\bar{\mathbf{f}}$ is a nonlinear function representing the state dynamics as modeled in designing the nominal trajectory. The nominal dynamics $\bar{\mathbf{f}}$ may be higher fidelity than the filter's dynamics $\mathbf{f}$. The vector $\boldsymbol{\upsilon}$ represents the dynamics modeled in the nominal trajectory but neglected in the filter models. In Kalman filtering, the difference between the true dynamics and the filter's dynamics is called process noise. Whereas these unmodeled dynamics are not actually white noise, they are modeled as such. The covariance of process noise is then tuned to achieve good performance. The same procedure is used here. To capture the difference between the two dynamical models, $\boldsymbol{\upsilon}$ is modeled as a zero-mean white process with spectral density $\hat{\mathbf{Q}}$. The goal is to represent the increased value of the navigation dispersion during propagation due to the difference between the nominal dynamical model and the filter's dynamical model.

The evolution of the navigation dispersion can be approximated to first order as

$$\delta\dot{\hat{\mathbf{x}}} = \dot{\hat{\mathbf{x}}} - \dot{\bar{\mathbf{x}}} = \mathbf{f}(\bar{\mathbf{x}} + \delta\hat{\mathbf{x}}) - \mathbf{f}(\bar{\mathbf{x}}) - \boldsymbol{\upsilon} \simeq \mathbf{F}(\bar{\mathbf{x}})\delta\hat{\mathbf{x}} - \boldsymbol{\upsilon} \tag{7}$$

The evolution of the navigation dispersion covariance is governed by

$$\dot{\hat{\mathbf{P}}} = \mathbf{F}(\bar{\mathbf{x}})\hat{\mathbf{P}} + \hat{\mathbf{P}}\mathbf{F}(\bar{\mathbf{x}})^T + \hat{\mathbf{Q}} \tag{8}$$

Similarly, the true state is modeled to evolve as

$$\dot{\mathbf{x}} = \mathbf{f}(\mathbf{x}) + \boldsymbol{\nu} \tag{9}$$

The evolution of the estimation error is given by

$$\begin{aligned}\dot{\mathbf{e}} &= \dot{\mathbf{x}} - \dot{\hat{\mathbf{x}}} \simeq \mathbf{f}(\bar{\mathbf{x}}) + \mathbf{F}(\bar{\mathbf{x}})(\mathbf{x} - \bar{\mathbf{x}}) + \boldsymbol{\nu} - \mathbf{f}(\bar{\mathbf{x}}) - \mathbf{F}(\bar{\mathbf{x}})(\hat{\mathbf{x}} - \bar{\mathbf{x}}) \\ &= \mathbf{F}(\bar{\mathbf{x}})\mathbf{e} + \boldsymbol{\nu}\end{aligned} \tag{10}$$

Vector $\boldsymbol{\nu}$ is modeled as zero-mean white noise with spectral density $\mathbf{Q}$. The onboard covariance $\mathbf{P}$ evolves as

$$\dot{\mathbf{P}} = \mathbf{F}(\bar{\mathbf{x}})\mathbf{P} + \mathbf{P}\mathbf{F}(\bar{\mathbf{x}}) + \mathbf{Q} \tag{11}$$

Notice that the Jacobian $\mathbf{F}$ could be evaluated at the estimated state $\hat{\mathbf{x}}$ instead of the nominal state $\bar{\mathbf{x}}$, as in the extended Kalman filter.

Finally,

$$\delta\dot{\mathbf{x}} = \dot{\mathbf{x}} - \dot{\bar{\mathbf{x}}} \simeq \mathbf{F}(\bar{\mathbf{x}})\delta\mathbf{x} + \boldsymbol{\nu} - \boldsymbol{\upsilon} \tag{12}$$

and $\bar{\mathbf{P}}$ evolves as

$$\dot{\bar{\mathbf{P}}} = \mathbf{F}(\bar{\mathbf{x}})\bar{\mathbf{P}} + \bar{\mathbf{P}}\mathbf{F}(\bar{\mathbf{x}}) + \bar{\mathbf{Q}} \tag{13}$$

Notice that $\bar{\mathbf{Q}} = \mathbf{Q} + \hat{\mathbf{Q}}$ if $\boldsymbol{\nu}$ and $\boldsymbol{\upsilon}$ are assumed to be uncorrelated.

Because the environment and navigation dispersions are naturally correlated, it is intuitive to create an augmented dispersion state for which the covariance is defined as Π

$$\Pi \triangleq E\left\{\begin{bmatrix}\delta\mathbf{x} \\ \delta\hat{\mathbf{x}}\end{bmatrix}\begin{bmatrix}\delta\mathbf{x} \\ \delta\hat{\mathbf{x}}\end{bmatrix}^T\right\} = \begin{bmatrix}\bar{\mathbf{P}} & \mathbf{C} \\ \mathbf{C}^T & \hat{\mathbf{P}}\end{bmatrix} \tag{14}$$

$$\mathbf{C} \triangleq E\{\delta\mathbf{x}\delta\hat{\mathbf{x}}^T\} \tag{15}$$

The evolution of the augmented covariance is given by

$$\dot{\Pi} = \begin{bmatrix}\mathbf{F}(\bar{\mathbf{x}}) & \mathbf{O}_{3\times3} \\ \mathbf{O}_{3\times3} & \mathbf{F}(\bar{\mathbf{x}})\end{bmatrix}\Pi + \Pi\begin{bmatrix}\mathbf{F}(\bar{\mathbf{x}}) & \mathbf{O}_{3\times3} \\ \mathbf{O}_{3\times3} & \mathbf{F}(\bar{\mathbf{x}})\end{bmatrix}^T + \begin{bmatrix}\bar{\mathbf{Q}} & \hat{\mathbf{Q}} \\ \hat{\mathbf{Q}} & \hat{\mathbf{Q}}\end{bmatrix} \tag{16}$$

where it is assumed that $\boldsymbol{\nu}$ and $\boldsymbol{\upsilon}$ are uncorrelated. All error states are modeled as first order Markov processes and are assumed to be uncorrelated to each other.

A. Rotation Conventions

The attitude is represented using a left rotation vector $\boldsymbol{\theta}$. Left rotations are used following the heritage from the space shuttle quaternion convention. The rotation vector represents the rotation from the inertial frame i to a body-fixed frame b. The corresponding rotation matrix $\mathbf{T}_i^b$ is found as

$$\mathbf{T}_i^b = \mathbf{T}(\boldsymbol{\theta}) = \mathbf{I}_{3\times 3} + \frac{\sin\theta}{\theta}[\boldsymbol{\theta}\times] + \frac{1-\cos\theta}{\theta^2}[\boldsymbol{\theta}\times]^2 \tag{17}$$

The attitude is the only state that is not integrated to obtain its nominal value. The attitude errors are defined in a multiplicative way:

$$\mathbf{T}(\delta\boldsymbol{\theta}) \triangleq \mathbf{T}(\boldsymbol{\theta})\mathbf{T}(\bar{\boldsymbol{\theta}})^T, \quad \mathbf{T}(\delta\hat{\boldsymbol{\theta}}) \triangleq \mathbf{T}(\hat{\boldsymbol{\theta}})\mathbf{T}(\bar{\boldsymbol{\theta}})^T, \quad \mathbf{T}(\mathbf{e}_\theta) \triangleq \mathbf{T}(\boldsymbol{\theta})\mathbf{T}(\hat{\boldsymbol{\theta}})^T \tag{18}$$

The attitude uncertainty is fixed and obtained from the deadband value. The attitude control system of the vehicle keeps the difference between the estimated attitude and the nominal attitude within a predetermined deadband. The root sum square navigation dispersion is therefore modeled as having a 3σ value equal to the deadband.

$$\hat{\mathbf{P}}_{\theta\theta} \triangleq E\{\delta\hat{\boldsymbol{\theta}}\delta\hat{\boldsymbol{\theta}}^T\} = \hat{\sigma}_\theta^2\mathbf{I}_{3\times 3} \tag{19}$$

The estimation error is modeled as zero-mean with covariance

$$\mathbf{P}_{\theta\theta} \triangleq E\{\mathbf{e}_\theta\mathbf{e}_\theta^T\} = \sigma_\theta^2\mathbf{I}_{3\times 3} \tag{20}$$

The estimation error is given by

$$\mathbf{T}(\mathbf{e}_\theta) = \mathbf{T}(\delta\boldsymbol{\theta})\mathbf{T}(\delta\hat{\boldsymbol{\theta}})^T \simeq \mathbf{T}(\delta\boldsymbol{\theta} - \delta\hat{\boldsymbol{\theta}}) \tag{21}$$

therefore,

$$\mathbf{P}_{\theta\theta} \triangleq E\{\delta\boldsymbol{\theta}\delta\boldsymbol{\theta}^T\} = \bar{\mathbf{P}}_{\theta\theta} + \hat{\mathbf{P}}_{\theta\theta} - E\{\delta\boldsymbol{\theta}\delta\hat{\boldsymbol{\theta}}^T\} - E\{\delta\hat{\boldsymbol{\theta}}\delta\boldsymbol{\theta}^T\} \tag{22}$$

where

$$E\{\delta\boldsymbol{\theta}\delta\hat{\boldsymbol{\theta}}^T\} = \hat{\mathbf{P}}_{\theta\theta} \tag{23}$$

which results in the attitude environment dispersions having covariance

$$\bar{\mathbf{P}}_{\theta\theta} = \mathbf{P}_{\theta\theta} + \hat{\mathbf{P}}_{\theta\theta} \tag{24}$$

B. Maneuvers

During the trans-Earth phase various maneuvers occur. They are grouped as either trans-Earth injections (TEI) or trajectory correction maneuvers (TCM), are modeled as impulsive, and provide an instantaneous change in the spacecraft's velocity. The translational maneuvers are introduced in LinCov as in [5].

The nominal orientation of the vehicle during Earth transfers is usually dictated by thermal, power, or communication constraints. From an optical navigation standpoint such orientations are not always ideal for measurement acquisition using star cameras. Therefore, if ground updates are not available, it is necessary to reorient the vehicle to acquire measurements and improve the state estimate before each translational maneuver. These corrections point the cameras toward the Earth or moon to collect the appropriate data. After a sufficient number of measurements are acquired the vehicle returns to its previous attitude. Because of uncoupled jet firings, these maneuvers increase the uncertainty in both the orientation and the velocity of the vehicle. Only the velocity uncertainty due to the rotational maneuvers is of interest here. The true change in velocity due to rotational maneuver $\Delta\mathbf{v}_r$ is modeled as

$$\Delta\mathbf{v}_r^i = \mathbf{T}_b^i\mathbf{b}_r + \boldsymbol{\zeta} \tag{25}$$

where $\mathbf{b}_r$ is a bias expressed in the body frame and $\boldsymbol{\zeta}$ is zero-mean white noise. The estimated perturbation is

$$\Delta\hat{\mathbf{v}}_r^i = \hat{\mathbf{T}}_b^i\hat{\mathbf{b}}_r \tag{26}$$

from which it is obtained that

$$\Delta\mathbf{v}_r^i - \Delta\hat{\mathbf{v}}_r^i \simeq \bar{\mathbf{T}}_b^i[\bar{\mathbf{b}}_r\times]\mathbf{e}_\theta + \bar{\mathbf{T}}_b^i\mathbf{e}_{b_r} + \boldsymbol{\zeta} \tag{27}$$

where $\bar{\mathbf{b}}_r$ is set to zero. Including only the active states,

$$\mathbf{x} = \begin{bmatrix}\mathbf{r}^T & \mathbf{v}^T & \boldsymbol{\theta}^T & \mathbf{b}_r^T\end{bmatrix}^T \tag{28}$$

the contribution to the estimation error from the rotational maneuvers is given by

$$\begin{aligned}\mathbf{e}^{+r} &= \mathbf{e}^{-r} + \begin{bmatrix}\mathbf{0}_{3\times 1}\\ \bar{\mathbf{T}}_b^i[\bar{\mathbf{b}}_r\times]\mathbf{e}_\theta + \bar{\mathbf{T}}_b^i\mathbf{e}_{b_r}\\ \mathbf{0}_{6\times 1}\end{bmatrix} + \begin{bmatrix}\mathbf{0}_{3\times 1}\\ \boldsymbol{\zeta}\\ \mathbf{0}_{6\times 1}\end{bmatrix}\\ &= (\mathbf{I}+\mathbf{E})\mathbf{e}^{-r} + \begin{bmatrix}\mathbf{0}_{3\times 1}\\ \boldsymbol{\zeta}\\ \mathbf{0}_{6\times 1}\end{bmatrix}\end{aligned} \tag{29}$$

where

$$\mathbf{E} = \begin{bmatrix}\mathbf{O}_{3\times 6} & \mathbf{O}_{3\times 3} & \mathbf{O}_{3\times 3}\\ \mathbf{O}_{3\times 6} & \bar{\mathbf{T}}_b^i[\bar{\mathbf{b}}_r\times] & \bar{\mathbf{T}}_b^i\\ \mathbf{O}_{3\times 6} & \mathbf{O}_{3\times 3} & \mathbf{O}_{3\times 3}\end{bmatrix} \tag{30}$$

As a result, the expression to update the covariance becomes

$$\mathbf{P}^{+r} = (\mathbf{I}+\mathbf{E})\mathbf{P}^{-r}(\mathbf{I}+\mathbf{E})^T + \mathbf{N} \tag{31}$$

The change in augmented dispersions covariance is given by

$$\begin{aligned}\Pi^{+r} &= \begin{bmatrix}\mathbf{I}+\mathbf{E} & \mathbf{O}_{12\times 12}\\ \mathbf{O}_{12\times 12} & \mathbf{I}+\mathbf{E}\end{bmatrix}\Pi^{-r}\begin{bmatrix}\mathbf{I}+\mathbf{E} & \mathbf{O}_{12\times 12}\\ \mathbf{O}_{12\times 12} & \mathbf{I}+\mathbf{E}\end{bmatrix}^T\\ &\quad + \begin{bmatrix}\mathbf{N} & \mathbf{O}_{12\times 12}\\ \mathbf{O}_{12\times 12} & \mathbf{O}_{12\times 12}\end{bmatrix}\end{aligned} \tag{32}$$

III. Filter Update

The optical measurements available to update the state in cislunar space are the star elevation from the planetary limb and the apparent planet radius, as shown in Fig. 1. LinCov update equations can be found in [5].

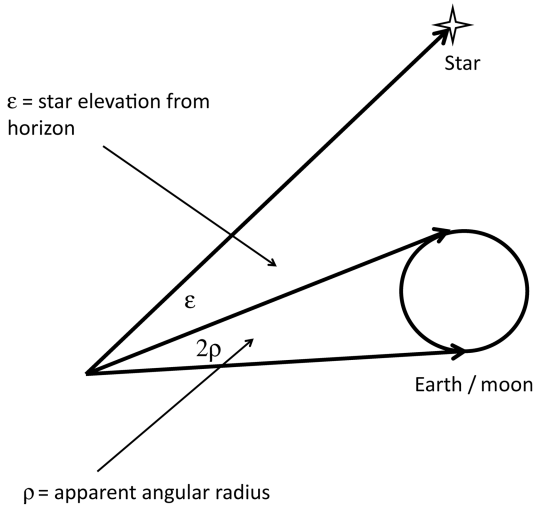

Fig. 1 Optical measurements available for cislunar navigation.

A. Star-Horizon Elevation Measurement

The model for the star-horizon measurement is based on Battin [6], but the measurement errors are different and introduced in alternative ways. Battin introduced an additive error, whereas in this work, three error contributions are accurately represented. All unit vectors derived in this section represent apparent directions, therefore aberration due to relative velocities are included. The apparent direction of the star, including stellar aberration, is given by

$$\mathbf{i}_s^* = \text{Unit}\left(\mathbf{i}_s + \frac{\mathbf{v}_{sv}}{c}\right) \tag{33}$$

Vector $\mathbf{v}_{sv}$ is the velocity of the vehicle with respect to the sun. The apparent direction of the horizon is given by

$$\mathbf{i}_h^* = \text{Unit}\left(\mathbf{i}_h + \frac{\mathbf{v}_{pv}}{c}\right) \tag{34}$$

where $\mathbf{v}_{pv}$ is the velocity of the vehicle with respect to the planet from which the elevation measurement is taken (Earth or moon).

Vector $\mathbf{r}_h$ is the position of the substellar point on the horizon [6] and,

$$\mathbf{i}_h = \text{Unit}(\mathbf{r}_h - \mathbf{r}) \tag{35}$$

defines the direction of the horizon with respect to the vehicle. The perfect star-elevation measurement ϵ is shown in Fig. 1 and can be expressed mathematically as

$$\epsilon = \arccos(\mathbf{i}_h^* \cdot \mathbf{i}_s^*) \tag{36}$$

Three error sources are modeled, each having both bias and noise. The first source of error is the precision of the star camera. The noise is η_{sc} and the bias is b_{sc}. The other two sources of error are shown in Fig. 2. Figure 2 represents a star camera snapshot as viewed by the spacecraft being outside the page. The second source of error is the identification of the substellar point along the planet's horizon, with bias b_{ss} and noise η_{ss}. Finally, there is the error in determining the altitude of the horizon for which the bias is b_h and noise is η_h. The measurement model is obtained using the cosine law and is given by

$$\begin{aligned} y_{se} = \Bigg\{ &\left(\epsilon + \arcsin\frac{R_p}{r_{pv}}\right)^2 + \left(\arcsin\frac{R_p}{r_{pv}} + \arcsin\frac{b_h + \eta_h}{r_{pv}}\right)^2 \\ &+ -2\left(\epsilon + \arcsin\frac{R_p}{r_{pv}}\right)\left(\arcsin\frac{R_p}{r_{pv}} + \arcsin\frac{b_h + \eta_h}{r_{pv}}\right) \\ &\times \cos(b_{ss} + \eta_{ss})\Bigg\}^{\frac{1}{2}} + b_{sc} + \eta_{sc} \end{aligned} \tag{37}$$

where r_{pv} is the distance between the planet and the vehicle and R_p is the local radius of the planet given by the distance between the center of the planet and the substellar point. The nominal measurement is given by

$$\begin{aligned} \bar{y}_{se} = \Bigg\{ &\left(\bar{\epsilon} + \arcsin\frac{R_p}{\bar{r}_{pv}}\right)^2 + \left(\arcsin\frac{R_p}{\bar{r}_{pv}} + \arcsin\frac{\bar{b}_h}{\bar{r}_{pv}}\right)^2 \\ &+ -2\left(\bar{\epsilon} + \arcsin\frac{R_p}{\bar{r}_{pv}}\right)\left(\arcsin\frac{R_p}{\bar{r}_{pv}} + \arcsin\frac{\bar{b}_h}{\bar{r}_{pv}}\right)\cos\bar{b}_{ss}\Bigg\}^{\frac{1}{2}} + \bar{b}_{sc} \end{aligned} \tag{38}$$

The measurement mapping matrix and the noise shaping matrix are defined as

$$\mathbf{H}_{se} = \left.\frac{\partial y_{se}}{\partial \mathbf{x}}\right|_{\mathbf{x}=\bar{\mathbf{x}},\boldsymbol{\eta}_{se}=\mathbf{0}} \qquad \mathbf{L}_{se} = \left.\frac{\partial y_{se}}{\partial \boldsymbol{\eta}_{se}}\right|_{\mathbf{x}=\bar{\mathbf{x}},\boldsymbol{\eta}_{se}=\mathbf{0}} \tag{39}$$

where

$$\boldsymbol{\eta}_{se} = \begin{bmatrix} \eta_{st} & \eta_{ss} & \eta_h \end{bmatrix}^T \tag{40}$$

and

$$\mathbf{R}_{se} = \mathbf{L}_{se} E\{\boldsymbol{\eta}_{se}\boldsymbol{\eta}_{se}^T\}\mathbf{L}_{se}^T. \tag{41}$$

B. Apparent Angular Radius Measurement

The sensed radius of the planet is corrupted by two errors: the horizon determination bias b_h and the horizon determination noise η_R.

$$R_{p,\text{meas}} = R_p + b_h + \eta_R \tag{42}$$

To characterize the measurement noise statistics, a simplified algorithm to determine the radius is used. The sensor software employs many points on the planet disk to determine the radius. For this analysis only three points are used. The assumption is that by using more points the error in reconstructing the planet radius decreases, but the shape of the curves stay the same. Hence this approach is more conservative, following the general theme of this analysis.

Let $\mathbf{p}_i = [x_i y_i]^T i = 1{:}3$ be three points that are not collinear. To find the coordinates of the center of a circle passing through the three points, the two chords passing through the points are used. The center is the interception between the two lines perpendicular to the chords and passing through the chords' midpoint. Mathematically the center is

$$x_c = \frac{m_a m_b(y_1 - y_3) + m_b(x_1 + x_2) - m_a(x_2 + x_3)}{2(m_b - m_a)} \tag{43}$$

$$y_c = \frac{(x_1 - x_3) + m_a(y_1 + y_2) - m_b(y_2 + y_3)}{2(m_a - m_b)} \tag{44}$$

where

$$m_a = \frac{y_2 - y_1}{x_2 - x_1} \qquad m_b = \frac{y_3 - y_2}{x_3 - x_2} \tag{45}$$

The order of the points is selected such that the denominators in Eq. (45) do not vanish. Once the center is known, the radius immediately follows as the distance between the center and any of the three points. The numerical data in Fig. 3 shows that the error in the radius estimate is not sensitive to the actual size of the planet. Let φ be the angle describing the arc of the planet disk inside the field of view. The three points are equally spaced along the arc. The error η_R is modeled as a function of φ and η_h:

$$\eta_R = f_1(\varphi, \eta_h) \tag{46}$$

Let σ_R be the standard deviation of η_R and σ_h be the standard deviation of η_h. To model σ_R, Monte Carlo runs are used. The location of

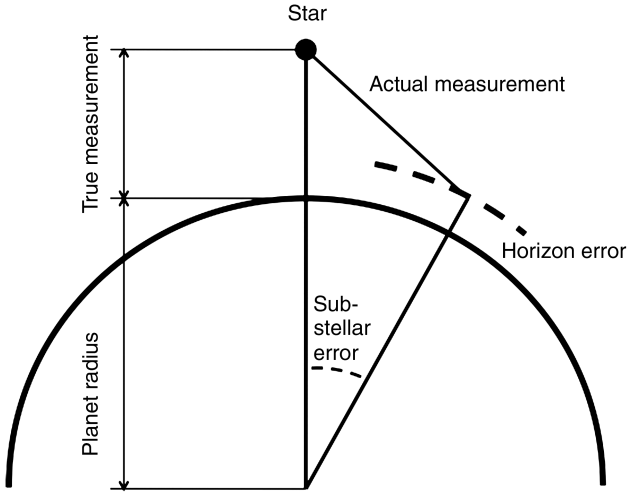

Fig. 2 Star-horizon elevation measurement errors.

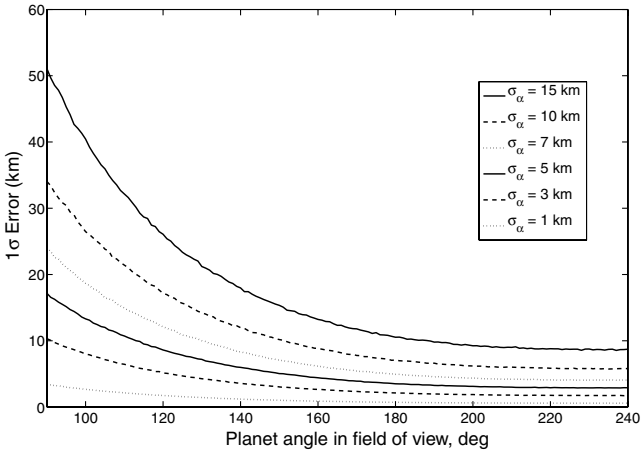

Fig. 3 Monte Carlo analysis of apparent angular radius measurement.

each point is corrupted with a zero-mean, Gaussian radial error with standard deviation ranging from 1 km to 15 km. There is no error in the position of the point along the arc. It is assumed that the length of the planet's arc inside the field of view ranges from 45 deg to 240 deg. There is no need to simulate arcs beyond 240 deg because in those cases the three points are still placed 120 deg apart.

Ten thousand Monte Carlo runs are considered for each case. Every run is based on a different circle center, location and error of the three points. Figure 3 shows the sample standard deviation for ranges between 90 and 240 deg. The sample mean is very close to zero.

From Fig. 3, it is observed that the curves are proportional to σ_h. Therefore, σ_R can be represented as

$$\frac{\sigma_R}{\sigma_h} = f_2(\varphi) \tag{47}$$

Function f_2 is expanded in series

$$f_2(\varphi) \simeq \sum_{i=0}^{n} c_i \varphi^{-i} \tag{48}$$

the coefficients c_i are obtained using least squares. For $n = 5$, the coefficients are determined as

$$\mathbf{c} = \begin{bmatrix} 1.8911 & -12.5306 & 33.3895 & -19.3107 & 5.7692 \end{bmatrix}^T \tag{49}$$

The apparent angular radius ρ is shown in Fig. 1 and can be expressed mathematically as

$$\rho = \arcsin\left(\frac{R_p}{r_{\text{vp}}}\right) \tag{50}$$

where $r_{\text{vp}} = \|\mathbf{r} - \mathbf{r}_p\|$ is the distance between the vehicle and the center of the planet. The angular radius measurement y_ρ is given by

$$y_\rho = \arcsin\left(\frac{R_p + b_h + \eta_R}{r_{\text{vp}}}\right) \tag{51}$$

The Jacobian is given by

$$\mathbf{H}_\rho(1{:}3) \triangleq \left.\frac{\partial y_\rho}{\partial \mathbf{r}}\right|_{\bar{\mathbf{x}}} = \frac{-R_p - \bar{b}_h}{\sqrt{1 - \left(\frac{R_p + \bar{b}_h}{\bar{r}_{\text{vp}}}\right)^2}} \frac{\bar{\mathbf{r}}^T - \mathbf{r}_p^T}{\bar{r}_{\text{vp}}^3} \tag{52}$$

$$\mathbf{H}_\rho(4) \triangleq \left.\frac{\partial y_\rho}{\partial b_h}\right|_{\bar{\mathbf{x}}} = \frac{1/\bar{r}_{\text{vp}}}{\sqrt{1 - \left(\frac{R_p + \bar{b}_h}{\bar{r}_{\text{vp}}}\right)^2}} \tag{53}$$

where $\mathbf{r}_p$ is the position of the planet. The indices 1 through 4 are used because only the active states are included in $\mathbf{x}^T = \begin{bmatrix} \mathbf{r}^T & b_h \end{bmatrix}$.

Hence, a Kalman filter that processes the measurement y_ρ employs Eq. (52) and (53) to obtain the measurement mapping matrix and

$$R_\rho = \frac{\sigma_h^2 / \bar{r}_{\text{vp}}^2}{1 - \left(\frac{R_p + \bar{b}_h}{\bar{r}_{\text{vp}}}\right)^2} \left(\sum_{i=0}^{n} c_i \varphi^{-i}\right)^2 \tag{54}$$

is the measurement covariance matrix.

C. Implementation

After the rotational maneuver, the vehicle is nominally oriented such that the edge of the Earth or moon is at the center of the star camera field of view (FOV). Two cases may arise: the angular radius of the planet as seen from the vehicle's position is either bigger than the FOV, or it is smaller. The first case is depicted in Fig. 4 in which an isosceles triangle is drawn with $b = c = \rho$ and $a = \text{FOV}$. All lengths are measured in radians because they correspond to apparent angles as seen by the camera. Using the cosine theorem

$$\cos\beta = \frac{a^2 + c^2 - b^2}{2ac} = \frac{\text{FOV}}{2\rho} \tag{55}$$

The smaller triangle in Fig. 4 is also isosceles, therefore it can be deduced that the semi-angle of the planet's arc inside the FOV $\varphi/2$ is

$$\varphi/2 = \frac{\pi - \beta}{2} \tag{56}$$

Figure 5 shows the case in which the angular radius of the planet is smaller than the star camera FOV. The angle β is still found using Eq. (55), and $\varphi/2$ is simply given by

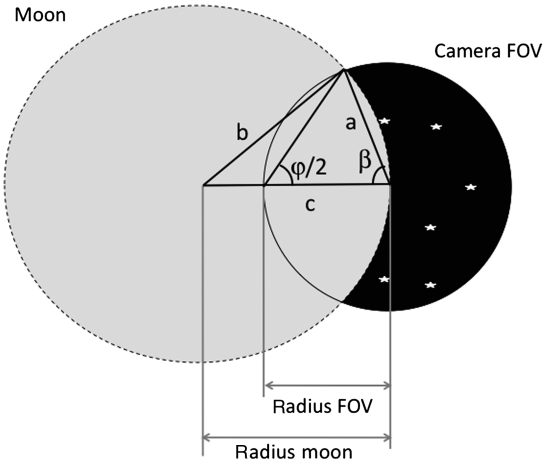

Fig. 4 Planet bigger than FOV.

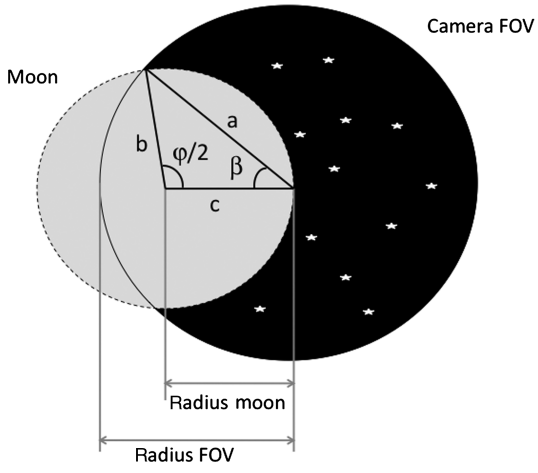

Fig. 5 Planet smaller than FOV.

Table 1 Nominal initial and final conditions

Parameter	Initial lunar orbit moon centered J2000	Conditions at EI Earth centered J2000
Universal time	2 Aug. 2018 02 17:16:10.0	7 Aug. 2018 07:59:59.7
ECI X position, m	$-1,834,714.32$	$-5,895,686.46$
ECI Y position, m	$-66,256.22$	$-1,734,099.86$
ECI Z position, m	$-73,974.33$	$-2,117,665.81$
ECI X velocity, m/s	-86.39	6,269.76
ECI Y velocity, m/s	813.94	$-8,032.14$
ECI Z velocity, m/s	1,413.63	8,665.97

$$\varphi/2 = \pi - 2\beta \tag{57}$$

If φ is greater than 240 deg it is set to 240 deg because the three points need to be equally spaced. This is consistent with the conservative approach selected because the FOV is likely square, and not circular, which increases its size.

D. Sensor Utilization

The strategy for sensor utilization is similar to that of ground updates. Ground updates occur before each maneuver to provide the targeting algorithm with the most reliable state estimate. Similarly, the star-elevation measurements occur in batches before each maneuver. Experience indicates that similar accuracies are obtained by performing all the measurements in a batch before the maneuver rather than equally distributing them along the trajectory. (The batch of measurements is taken before the errors grow enough to violate the linearization hypothesis of the Kalman filter.) For this particular application, it is advantageous to take the measurement in batches because it minimizes the number of slews. Because each slew adds dispersions to the trajectory, it is desirable to have as few as possible.

The number of measurements taken for each batch is determined to ensure steady state is attainable. In this case, steady state implies that additional measurements do not further reduce the covariance, but only cancel the process noise effect.

There is a 50 h period between the first and second midcourse correction. The navigation covariance grows too large if no update is performed during this period. Therefore, two batches of measurements are taken between the first and second midcourse correction.

IV. Lincov Parameters

This section contains all the parameters used in the LinCov run. The parameters are chosen as representative of the Orion lunar return, which is used as the case study to validate the developed navigation strategy.

A. Nominal Trajectory

The nominal trajectory has initial and final conditions given in Table 1. The nominal Orion attitude during transfers between Earth and moon has the engines pointing toward the sun to maximize the solar arrays' energy production and for other thermal advantages. The vehicle's attitude is not integrated, but the nominal orientation always points the engines toward the sun.

B. Errors and Dispersions

The initial environment dispersions and estimation errors are chosen to have the same numerical values and are shown in Table 2. The error components are given in the local vertical local horizontal frame (LVLH). The LVLH frame is defined with the z-axis along the position vector pointing downward toward the center of the Earth. The x-axis points in the same direction as the velocity vector. The y-axis completes the right-orthogonal triad.

The 3σ root sum square navigation dispersion in attitude is modeled as being equal to the attitude deadband, which is 20 deg. The attitude navigation error is 0.1 deg, as shown in Table 3.

Table 2 Initial state variances

State	Standard deviation
LVLH X position, m	1603
LVLH Y position, m	333
LVLH Z position, m	1000
LVLH X velocity, m/s	0.9466
LVLH Y velocity, m/s	0.5
LVLH Z velocity, m/s	1.61

Table 3 Attitude variances

Standard deviation	Value
$\hat{\sigma}_\theta$, deg	$20/(3\sqrt{3})$
σ_θ, deg	0.1

Table 4 Process noise values

Error type	Value
Active ($\mu g\sqrt{s}$)	20
Quiescent ($\mu g\sqrt{s}$)	2

Table 5 Quiescent time schedule

Begin quiescent time	End quiescent time
TEI $-$ 1 + 3 h	TEI $-$ 1 + 11 h
TEI $-$ 3 + 3.5 h	TEI $-$ 3 + 11.5 h
TEI $-$ 3 + 25 h	TEI $-$ 3 + 33 h
TEI $-$ 3 + 47 h	TEI $-$ 3 + 55 h
EI $-$ 14 h	EI $-$ 7 h

Table 6 Star-elevation measurement errors, all values 1σ

Sensor	Error type	Moon	Earth
Star camera	η_{sc}, arcsec	5	5
——	b_{sc}, arcsec	3.33	3.33
Stellar subpoint	η_{ss}, arcsec	5	10
——	b_{ss}, arcsec	2	5
Horizon	η_h, km	5	10
——	b_h, km	3	3

C. Process and Measurement Noise

The Orion vehicle is required to have quiescent times in which all possible trajectory perturbing activities are reduced to a minimum. These periods mostly coincide with the astronauts' sleeping schedule. In this simulation, two values of process noise are used, one for active periods and one for quiescent, as shown in Table 4. Table 5 shows the quiescent time schedule.

Table 7 Trans-Earth nominal maneuver sequence

Maneuver	Time, h	Nominal $\Delta\mathbf{v}$, m/s
TEI-1	2.68	[439.00 − 255.15 − 261.37]
TEI-2	17.84	[29.38 100.42 − 96.05]
TEI-3	26.73	[264.62 − 206.67 23.27]
TCM-1	44.73	[0 0 0]
TCM-2	94.73	[0 0 0]
TCM-3	105.73	[0 0 0]

Table 8 Trans-Earth maneuver errors, all values 1σ

Error type	Value
Misalignment, deg	0.01
Bias, m/s	0.001
Scale factor, ppm	10
Noise, m/s	0.001

Table 6 shows the measurement noise standard deviations. The values used for the horizon and substellar point errors are those of the Apollo missions.

D. Maneuvers Errors

Table 7 shows the six planned maneuvers during Earth return. The vehicle departs the vicinity of the moon through a sequence of three TEI maneuvers. Three TCMs are also performed. Times are expressed as hours from the beginning of the simulation which occurs 1.11 days before TEI-3. Table 8 shows the maneuver errors used in the simulation (all values are 1σ per axis).

V. Event Triggers

Using linear covariance techniques, events are usually time driven. Some events, like EI, are naturally defined by the state and not by time. The technique to introduce these events into LinCov is that presented in reference [7] with some modifications due to the fact that the event is triggered by the true state and not by the navigated state.

The event is defined by some function of the true state:

$$\Psi(\mathbf{x}) = 0 \tag{58}$$

The true state at the true event time (t_e) differs from the nominal state at the nominal event time ($\bar{t}_e$) because of differences in both state and time:

$$\mathbf{x}(t_e) \simeq \mathbf{x}(\bar{t}_e) + \dot{\mathbf{x}}(\bar{t}_e)[t_e - \bar{t}_e] \tag{59}$$

$$\hat{\mathbf{x}}(t_e) \simeq \hat{\mathbf{x}}(\bar{t}_e) + \dot{\hat{\mathbf{x}}}(\bar{t}_e)[t_e - \bar{t}_e] \tag{60}$$

where

$$\dot{\mathbf{x}}(\bar{t}_e) = \dot{\bar{\mathbf{x}}}(\bar{t}_e) + \delta\dot{\mathbf{x}}(\bar{t}_e) \tag{61}$$

$$\dot{\hat{\mathbf{x}}}(\bar{t}_e) = \dot{\bar{\mathbf{x}}}(\bar{t}_e) + \delta\dot{\hat{\mathbf{x}}}(\bar{t}_e) \tag{62}$$

Expanding Eq. (58),

$$0 = \Psi(\bar{\mathbf{x}}(\bar{t}_e)) + \Psi_x[\delta\mathbf{x}(\bar{t}_e) + \dot{\bar{\mathbf{x}}}(\bar{t}_e)\delta t_e] \tag{63}$$

where

$$\Psi_x \triangleq \left.\frac{\partial\Psi}{\partial\mathbf{x}}\right|_{\bar{\mathbf{x}}} \qquad \delta t_e \triangleq t_e - \bar{t}_e \tag{64}$$

Noticing that $\Psi(\bar{\mathbf{x}}(\bar{t}_e)) = 0$ and solving for δt_e,

$$\delta t_e = -\frac{\Psi_x\delta\mathbf{x}(\bar{t}_e)}{\Psi_x\dot{\bar{\mathbf{x}}}(\bar{t}_e)} \tag{65}$$

substituting the preceding expression into Eqs. (59) and (60) using Eqs. (61) and (62), and neglecting second-order terms leads to

$$\mathbf{x}(t_e) \simeq \mathbf{x}(\bar{t}_e) - \dot{\bar{\mathbf{x}}}(\bar{t}_e)\frac{\Psi_x\delta\mathbf{x}(\bar{t}_e)}{\Psi_x\dot{\bar{\mathbf{x}}}(\bar{t}_e)} \tag{66}$$

$$\hat{\mathbf{x}}(t_e) \simeq \hat{\mathbf{x}}(\bar{t}_e) - \dot{\hat{\mathbf{x}}}(\bar{t}_e)\frac{\Psi_x\delta\mathbf{x}(\bar{t}_e)}{\Psi_x\dot{\bar{\mathbf{x}}}(\bar{t}_e)} \tag{67}$$

Matrix $\mathbf{U}$ is defined as

$$\mathbf{U} \triangleq \frac{\dot{\bar{\mathbf{x}}}(\bar{t}_e)\Psi_x}{\Psi_x\dot{\bar{\mathbf{x}}}(\bar{t}_e)} \tag{68}$$

The difference between the true/estimated state at the time of the event and the nominal state at the nominal time of the event is given by

$$\delta\mathbf{x}(t_e) = \mathbf{x}(t_e) - \bar{\mathbf{x}}(\bar{t}_e) = (\mathbf{I} - \mathbf{U})\delta\mathbf{x}(\bar{t}_e) \tag{69}$$

$$\delta\hat{\mathbf{x}}(t_e) = \hat{\mathbf{x}}(t_e) - \bar{\mathbf{x}}(\bar{t}_e) = \delta\hat{\mathbf{x}}(\bar{t}_e) - \mathbf{U}\delta\mathbf{x}(\bar{t}_e) \tag{70}$$

$$\mathbf{e}(t_e) = \mathbf{e}(\bar{t}_e) \tag{71}$$

Therefore, the estimation error remains approximately unchanged (approximation good to first order). Notice that t_e is a random variable and not a deterministic time. The dispersions are still unbiased [7]. Thus, the augmented covariance at the event (no precise time can be attributed to this covariance) is given by

$$\Pi_e = \begin{bmatrix} \mathbf{I} - \mathbf{U} & \mathbf{O} \\ -\mathbf{U} & \mathbf{I} \end{bmatrix} \Pi(\bar{t}_e) \begin{bmatrix} \mathbf{I} - \mathbf{U} & \mathbf{O} \\ -\mathbf{U} & \mathbf{I} \end{bmatrix}^T \tag{72}$$

Entry interface is defined as a constant altitude $h_{\mathrm{EI}} = 400{,}000$ feet; therefore, the function Ψ is equal to

$$\Psi = \mathbf{r}^T\mathbf{r} - (h_{\mathrm{EI}} + R_{\mathrm{EARTH}})^2 = 0 \tag{73}$$

Vector $\bar{\mathbf{x}}_{\mathrm{EI}}$ is the nominal state at EI. Matrix $\mathbf{U}$ at EI is

$$\mathbf{U}_{\mathrm{EI}} = \frac{1}{\bar{\mathbf{r}}_{\mathrm{EI}}^T\bar{\mathbf{v}}_{\mathrm{EI}}}\begin{bmatrix} \dot{\bar{\mathbf{x}}}_{\mathrm{EI}}\bar{\mathbf{r}}_{\mathrm{EI}}^T & \mathbf{O} \end{bmatrix} \tag{74}$$

Notice that there is no radial uncertainty in the environment dispersion because the environment dispersion is perpendicular to $\bar{\mathbf{r}}_{\mathrm{EI}}$:

$$\bar{\mathbf{r}}_{\mathrm{EI}}^T\delta\mathbf{r}_{\mathrm{EI}} = \bar{\mathbf{r}}_{\mathrm{EI}}^T(\mathbf{I} - \frac{\bar{\mathbf{v}}_{\mathrm{EI}}\bar{\mathbf{r}}_{\mathrm{EI}}^T}{\bar{\mathbf{r}}_{\mathrm{EI}}^T\bar{\mathbf{v}}_{\mathrm{EI}}})\delta\mathbf{r}(\bar{t}_{\mathrm{EI}}) = (\bar{\mathbf{r}}_{\mathrm{EI}}^T - \bar{\mathbf{r}}_{\mathrm{EI}}^T)\delta\mathbf{r}(\bar{t}_{\mathrm{EI}}) = 0 \tag{75}$$

This is to be expected because the altitude is fixed and equal to h_{EI} at the event.

VI. Results

In this section, the results of various numerical simulations are shown. Targeting occurs approximately 45 min before the maneuver. In this simulation, the vehicle is rotated to acquire measurements 2 h before the maneuver and takes 60 measurements 1 min apart. Measurement acquisition also occurs between the second and third midcourse correction, more precisely at 60 and 80 h from the beginning of the simulation.

The single most important parameter to assure crew safety during entry is the flight-path angle γ:

$$\gamma = \arcsin\frac{\mathbf{r}^T\mathbf{v}}{\|\mathbf{r}\|\|\mathbf{v}\|} \tag{76}$$

The flight-path angle error covariance is approximately given by

$$P_{\gamma\gamma}(t) = \Gamma(\mathbf{x})\mathbf{P}(t)\Gamma(\mathbf{x})^T \tag{77}$$

where $\Gamma \triangleq \frac{\partial\gamma}{\partial\mathbf{x}}$. The nonzero partials of the flight-path angle are given by:

$$\begin{aligned}\frac{\partial\gamma}{\partial\mathbf{r}} &= \frac{1}{\cos\gamma}\frac{\mathbf{v}^T}{\|\mathbf{r}\|\|\mathbf{v}\|}\left(\mathbf{I} - \frac{\mathbf{r}\mathbf{r}^T}{\|\mathbf{r}\|^2}\right)\\ \frac{\partial\gamma}{\partial\mathbf{v}} &= \frac{1}{\cos\gamma}\frac{\mathbf{r}^T}{\|\mathbf{r}\|\|\mathbf{v}\|}\left(\mathbf{I} - \frac{\mathbf{v}\mathbf{v}^T}{\|\mathbf{v}\|^2}\right)\end{aligned} \tag{78}$$

Notice that the flight-path angle uncertainty at each given time is not of interest. The important quantity is the uncertainty mapped to EI. For example, if at the time of the last maneuver the flight-path angle onboard uncertainty mapped to EI is 0.5 deg 3σ, a better environment dispersion cannot be achieved than that at EI. The uncertainty actually increases due to acceleration perturbations, maneuver errors, targeting errors, etc. Therefore, there are two values of interest: the onboard uncertainty at the time the last maneuver is targeted, and the environment dispersion at EI. The first is a factor in determining if the vehicle can be safely guided to EI, the second tells whether the safety conditions are met.

The plots presented in this section show the flight-path angle error mapped to EI. This is done by propagating the covariance matrix to the final time with the state transition matrix and evaluating the partial derivatives at the nominal value at EI. Let $P_{\gamma\gamma}(t_{\mathrm{EI}}, t)$ denote the onboard variance of the flight-path angle error mapped to EI. From Eq. (77) it follows that

$$P_{\gamma\gamma}(t_{\mathrm{EI}}, t) = \Gamma_{\mathrm{EI}}\Phi(t_{\mathrm{EI}}, t)\mathbf{P}(t)\Phi(t_{\mathrm{EI}}, t)^T\Gamma_{\mathrm{EI}}^T \tag{79}$$

where $\Gamma_{\mathrm{EI}} = \Gamma(\bar{\mathbf{x}}_{\mathrm{EI}})$. Similarly,

$$\begin{aligned}\bar{P}_{\gamma\gamma}(t_{\mathrm{EI}}, t) = \Gamma_{\mathrm{EI}}(\mathbf{I}_{n\times n} - \mathbf{U}_{\mathrm{EI}})\Phi(t_{\mathrm{EI}}, t)\bar{\mathbf{P}}(t)\Phi(t_{\mathrm{EI}}, t)^T(\mathbf{I}_{n\times n}\\ - \mathbf{U}_{\mathrm{EI}})^T\Gamma_{\mathrm{EI}}^T\end{aligned} \tag{80}$$

Figures 6 and 7 show the numerical results. It can be seen that the navigation system meets the requirements because the navigation error at the time of the last maneuver is less than 0.5 deg 3σ and the environment dispersion at EI is less than 1 deg 3σ.

Figure 6 shows the variance of the flight-path angle estimation error mapped to EI. Two hours before each translational maneuver the uncertainty decreases because the measurements are acquired. The last two measurements from the moon's horizon (at times 60 and 80 h) do not contribute as much because most of the information has already been extracted.

Figure 7 shows the variance of the flight-path angle environment dispersion mapped to EI. At each maneuver the uncertainty decreases. Notice that the sudden drop in uncertainty is due to the fact that the error is mapped to EI. By plotting the error at the current time without mapping it to EI the uncertainty decreases gradually. The behavior occurring after the last TEI maneuver is also due to the way the data are plotted. After that maneuver the uncertainty projected to EI is very low. It seems that the uncertainty increases very rapidly right after that. This is because the errors are projected to EI. By plotting the errors at the current time, the error increases more gradually and is due to the geometry of the problem.

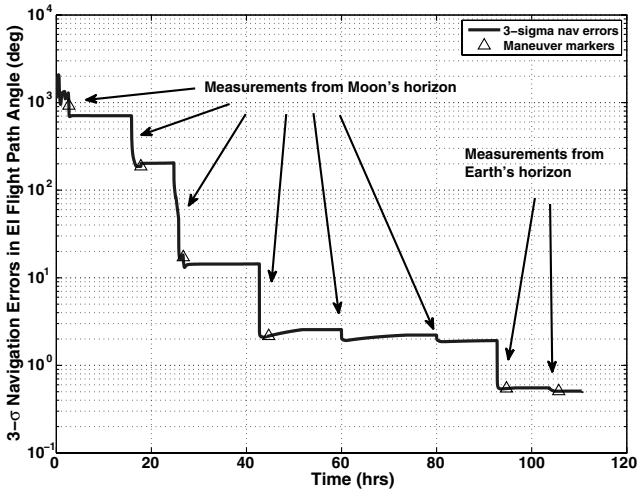

Fig. 6 Onboard flight-path angle error mapped to EI.

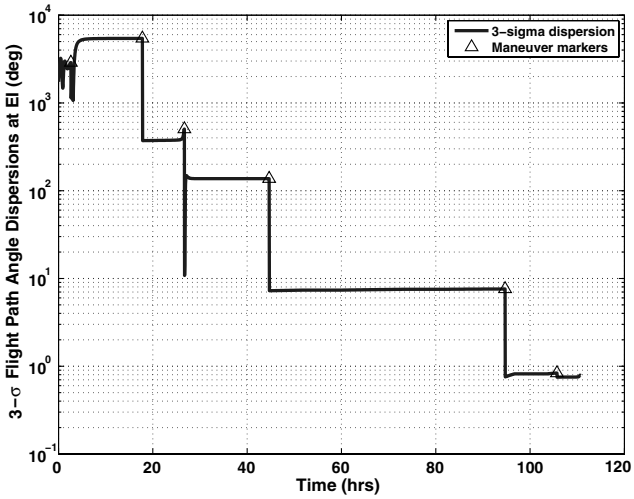

Fig. 7 True flight-path angle dispersion mapped to EI.

There is one final comment on the two plots. It seems that the uncertainty remains quite constant in between drops, suggesting small values of process noise. In fact, position and velocity uncertainty grows rapidly. For example, position uncertainty is on the order of tens of kilometers. However, it takes large changes in position and velocity errors to produce appreciable changes in flight-path angle error.

VII. Conclusions

A new onboard system for autonomous midcourse navigation is proposed and analyzed. Optical measurements are used to achieve autonomy. The measurements chosen are the elevation of a known star from the Earth or moon's horizon and the apparent angular radius of the planetary body. New models are developed to describe both measurement types. These models include different error sources and the statistical properties of the measurement error are confirmed with the aid of Monte Carlo methods.

A navigation strategy is developed to achieve the desired flight-path angle accuracy. Either the Earth or moon needs to be inside the camera's field of view to obtain a measurement. The nominal attitude of the vehicle does not guarantee visibility of the two bodies. Slew maneuvers are prescribed to obtain a batch of measurements before the targeting of each translational maneuver. These maneuvers increase the environment dispersion due to imperfect coupling of the jet firings.

Linear covariance analysis techniques with realistic models of the guidance, navigation, and control system, as well as the true dynamics, are used to obtain statistical properties of the navigation error and of the trajectory dispersions. These statistical properties are used to verify the proposed autonomous navigation system design. The success of the navigation system is measured against safety requirements. A direct Earth entry requires flight-path angle accuracy at EI of ± 1 deg. Therefore, the flight-path angle environment dispersion must be less than 1 deg. Half of this uncertainty is allocated to the navigation system, with the other half being allocated to targeting, control, unmodeled dynamics, etc. The results indicate that the proposed architecture is a viable solution for an autonomous midcourse navigation system because all the requirements are met. The navigation errors at the time of the last midcourse maneuver provide an EI flight-path angle accuracy of

more than 0.5 deg 3σ. The environment dispersions at EI are less than 1 deg 3σ.

Acknowledgment

The author is very grateful to Chris D'Souza at NASA Johnson Space Center for developing and making available many of the tools used to produce the LinCov runs.

References

[1] Hill, K., and Born, G. H., "Autonomous Orbit Determination from Lunar Halo Orbits Using Crosslink Range," *Journal of Spacecraft and Rockets*, Vol. 45, No. 3, May–June 2008, pp. 548–553. doi:10.2514/1.32316

[2] Psiaki, M. L., and Hinks, J. C., "Autonomous Lunar Orbit Determination using Star Occultation Measurements," Guidance Navigation and Control Conference and Exhibit, Hilton Head, SC, AIAA Paper 2007-6657, 2007.

[3] Tuckness, D. G., and Young, S.-Y., "Autonomous Navigation for Lunar Transfer," *Journal of Spacecraft and Rockets*, Vol. 32, No. 2, Mar.–Apr. 1995, pp. 279–285. doi:10.2514/3.26607

[4] Mayback, P. S., "Stochastic Models, Estimation, and Control," Vol. 1, *Mathematics in Science and Engineering*, Academic Press, Orlando, FL, 1979.

[5] Geller, D. K., "Linear Covariance Techniques for Orbital Rendezvous Analysis and Autonomous Onboard Mission Planning," *Journal of Guidance, Control, and Dynamics*, Vol. 29, No. 6, Nov.–Dec. 2006, pp. 1404–1414. doi:10.2514/1.19447

[6] Battin, R. H., *An Introduction to the Mathematics and Methods of Astrodynamics*, AIAA Education Series, AIAA, New York, 1987.

[7] Geller, D. K., Rose, M. B., and Woffinden, D. C., "Event Triggers in Linear Covariance Analysis with Applications to Orbital Rendezvous," *Journal of Guidance, Control, and Dynamics*, Vol. 32, No. 1, Jan.–Feb. 2009, pp. 102–111. doi:10.2514/1.36834

B. Marchand
Associate Editor